CrossMark

RESEARCH PAPER

Seed-mediated synthesis of acanthosphere-like gold microstructures with tunable LSPR in the NIR region using gemini surfactants as directing agents for SERS applications

Yan Xia · Zhinong Gao (ID) **· Xueming Liao · Wanying Wei · Chenchen Pan**

Abstract Acanthosphere-like gold microstructures (AGMs) were synthesized using a facile, two-step, seed-mediated method and butanediyl-1,4-*bis*(dimethylhexadecylammonium bromide) (16-4-16) as a structure-directing agent. The morphologies and sizes of the products were controlled during the synthesis process by adjusting the concentrations of 16-4-16, the $AgNO_3$ feed, $HAuCl_4$, ascorbic acid, the amount of Ag seeds and the types of gemini surfactants used through systematic inquiry; particle sizes ranging from 130 to 800 nm were well prepared. Correspondingly, the morphology of the products changed between regular and irregular AGMs, and the products presented a number of new morphologies, such as open-mouthed submicrostructures and ribbon nanowires. In particular, with the increase in the 16-4-16 concentration, the structural morphology of the thorns clearly changed from a tip to a lamellar structure. A UV-vis spectroscopic analysis indicated that the localized surface plasmon resonance (LSPR) peak of the AGMs could be adjusted by changing the above factors, which extended from 500 to 1350 nm in the near-infrared (NIR) region, enabling a tremendous potential for using the AGMs as platforms for various biomedical applications. Based on the intermediate products, we propose a two-stage growth mechanism for the AGMs in which their solid cores and tips are generated successively. Surface-enhanced Raman scattering (SERS) measurements indicate that the AGMs can serve as sensitive SERS substrates; a SERS detection limit of 5×10^{-7} M is presented for rhodamine B molecules.

Keywords Seed mediated · Gold microstructures · Gemini surfactants · Localized surface plasmon resonance · Nanoparticles · Biomedical applications

Y. Xia · Z. Gao (✉) · X. Liao · W. Wei · C. Pan
College of Chemistry and Molecular Sciences, Wuhan University, Wuhan 430072 Hubei, People's Republic of China
e-mail: gzn@whu.edu.cn

Y. Xia · Z. Gao · X. Liao · W. Wei · C. Pan
Key Laboratory of Biomedical Polymers, Ministry of Education of China, Wuhan 430072 Hubei, People's Republic of China

Introduction

Gold nanoparticles (NPs) with well-defined nanostructures have various novel physical, chemical, biological and electronic properties that are extensively applied in plasmon-enhanced spectroscopies (Nepal et al. 2013), biosensors (Guo et al. 2013), drug carriers (Wang et al. 2013a, b, c), catalysis (Ke et al. 2014) and imaging (Liu et al. 2014c, b, c). Gold NPs have highly distance-dependent optical properties and extremely high extinction coefficients (Wang and Ma 2009). Thus far, various gold nanoparticles with different well-controlled morphologies have been developed, including nanoparticles (Chen et al. 2016), nanowires (Xu et al. 2014), nanorods (Xu et al. 2015), nanoplates (Chen et al. 2014), nanoflowers (Jiji and Gopchandran 2015) and

Springer

nanourchins (Sabri et al. 2016). Thanks to their distinct morphology and optical properties, multibranched gold nanoparticles have attracted particular attention (Vijayaraghavan et al. 2016). There is an urgent need for materials with extinction coefficients in the near-infrared (NIR) region (Rengan et al. 2015), especially in the first (650–950 nm) and second biological windows (1000–1350 nm). In the literature, few materials have been reported without branched structures that have absorption peaks within these two windows (Zaleska-Medynska et al. 2016). These extinction coefficients can be more easily realized using multibranched nanomaterials. However, highly branched structures are more difficult to synthesize reproducibly as they are more complicated structures that are usually polycrystalline with diverse crystal domains between the core and branches.

In the past few decades, scientists have begun to focus on controlling the synthesis of highly branched structures with good monodispersity. Sau et al. first reported the synthesis of multipods of metallic particles by reducing gold salts in the presence of hexadecyl trimethyl ammonium bromide (CTAB) (Sau and Murphy 2004). Years later, urchin-like gold nanoparticles were synthesized by Bakr et al. (2006), and they exhibited a more regular multibranched nanostructure morphology. Thereafter, many efforts have been devoted to developing simpler methods for controlling the synthesis of multibranched gold, silver or alloyed nanoparticles, such as the chemical reduction method (Wang et al. 2012), hydrothermal method (Liang et al. 2008), double-sided tape-assisted transfer method (Liu et al. 2014a, b, c), interface method (You et al. 2012), aqueous synthesis method (Cheng et al. 2014), electrochemical method (Zhou et al. 2013), particle-mediated method (Fang et al. 2010; Liu et al. 2013; You and Fang 2016) and seed-mediated method (Li et al. 2011; Liu et al. 2014a, b, c; Lu et al. 2008; Xu et al. 2010). Among these methods, the seed-mediated method is unique for the synthesis of inorganic NPs because it can be used to easily control the shape, composition and structure of nanoparticles. In addition, this method can be conveniently conducted in a quantitative manner (Gilroy et al. 2016). Selecting suitable surfactants as the directing agents during the synthesis of nanomaterials is tremendously important for the seed-mediated method. The surfactant can prevent the products from forming deposits and enable effective control of the nanoparticle morphology (Bakshi 2016). However, in the literature,

the frequent use of surfactants has been limited to a few conventional surfactants, such as CTAB (Wu et al. 2009), sodium citrate (Han et al. 2012) and polyvinyl-pyrrolidone (PVP) (Niu et al. 2015). Compared with traditional surfactants, gemini surfactants have a lower critical micelle concentration (CMC) and surface tension (Menger and Littau 1991) and can more easily form various types of micelles (Samik Hait and Moulik 2002; Wang et al. 2013a, b, c). For gemini surfactants, changing the head and tail group chemical structures (Jain et al. 2014) and spacer length (Bhattacharya and Biswas 2011; Xu et al. 2014) easily adjusts the morphology of the micelles and thus affects the morphology of the nanoparticles. Based on the above reasons, gemini surfactants have more advantages for regulating the synthesis of nanoparticles (Bhattacharya and Biswas 2011; Guerrero-Martinez et al. 2009; Song et al. 2012) and are expected to play an important role during the preparation of new nanomaterials.

In this article, with the assistance of a gemini surfactant, we utilize a two-step, seed-mediated growth method to synthesize AGMs (spherical microparticles with a high density of tips on the surface) in high yield. We control the size and morphology of the products by regulating the concentration of butanediyl-1,4-bis(dimethylhexadecylammonium bromide) (16-4-16), AgNO$_3$ feed, HAuCl$_4$ and ascorbic acid (AA), the amount of Ag seed and the types of gemini surfactants used (16-s-16, s = 4, 6, 10 and 12, where 16 and s stand for the carbon atom number in the tail alkyl chain and the methylene spacer, respectively). The UV-vis spectroscopic analysis shows that the localized surface plasmon resonance (LSPR) peak of the AGMs can be readily adjusted by changing the above parameters, which extends from 500 to 1350 nm in the NIR region. This system is a potential platform for a tremendous variety of biomedical applications. With the use of gemini surfactants as stabilizers, the seed preparation does not require boiling, and the growth process can be completed in 30 min. In spite of the synthetic methods reported, a comprehensive study of the mechanism of formation is still lacking. We comprehensively discuss the role of the gemini surfactants during the product formation as a function of the concentration and surfactant type. Furthermore, we provide a probable growth mechanism for the AGMs according to the data from the intermediates in which the solid cores and tips are established sequentially rather than simultaneously. In addition, the surface-enhanced Raman scattering (SERS) properties

of the AGMs are investigated by applying rhodamine B (RhB) as an indicator molecule, and a low detection limit is reported (5×10^{-7} M).

Experimental section

Materials

Silver nitrate (AgNO$_3$, ≥99.8%), sodium tetrahydroborate (NaBH$_4$, 98%), hydrogen tetrachloride(III) tetrahydrate (HAuCl$_4$·4H$_2$O, ≥ 99.99%), rhodamine B (RhB, ≥97.5%) and ascorbic acid (AA, ≥99.7%) were obtained from Sinopharm Chemical Reagent Corporation. All chemicals were of analytical grade and used without further purification. The cationic gemini surfactants (16-s-16, s = 4, 6, 10 and 12) used herein were synthesized and purified according to a previous report (Zana et al. 1991). Ultrapure water (18.25 MΩ cm) was created in a Milli-Q system and was used to prepare all solutions.

Characterization techniques

The products were characterized using field emission scanning electron microscopy (FE-SEM, Zeiss Sigma FESEM, 20 KV), UV-vis spectroscopy (Shimadzu, UV-3600), powder X-ray diffraction (XRD, PANalytical X'pert Pro, 40 kV), transmission electron microscopy (TEM, JEM-2100, 200 kV), selected-area electron diffraction (SAED) and energy-dispersive X-ray spectroscopy (EDS). Dynamic light-scattering (DLS) measurements were recorded using a Zetasizer Nano (ZEN 3600, Malvern Instruments). Raman scattering signals were collected using Ar$^+$ laser excitation at 514.5 nm from a Renishaw RM1000 Raman spectrophotometer.

Synthesis of the silver seeds

Silver seeds were prepared by reducing AgNO$_3$ using NaBH$_4$. Briefly, 100 μL of 10 mM AgNO$_3$ was added to 8 mL of 5 mM 16-4-16. Then, 300 μL of an ice-cold 10 mM NaBH$_4$ solution was injected into the mixed solution with vigorous stirring. Stirring was maintained for 10 min in a water bath (30 °C) to initiate the formation of quasispherical Ag nanoparticles.

Growth of the AGMs

Scheme 1 presents a brief summary of the synthesis procedure. Two 50-mL vials were labelled A and B. Then, 8 mL of 5 mM 16-4-16 was added to these vials. Next, sample A was prepared by sequentially adding 500 μL of the silver seed solution, 450 μL of 4 mM AgNO$_3$, 1 mL of 1% (w/w) HAuCl$_4$ and 500 μL of 100 mM AA with vigorous stirring. Then, after stirring and keeping the solution undisturbed for 30 s, 500 μL of the solution in A was removed (to act as the seed for B) and added to B rapidly. The remaining solutions were prepared using the same procedure for A. Finally, B was allowed to stand in a water bath at 30 °C for 30 min. The target product was gathered by centrifugation at 3000 rpm, using a rotational radius of 6.5 cm (g = 654 N), for 4 min to remove the unreacted reagents. The precipitate was redispersed into ultrapure water and centrifuged three times. Finally, the AGMs were diluted with 3 mL of deionized water for further analysis.
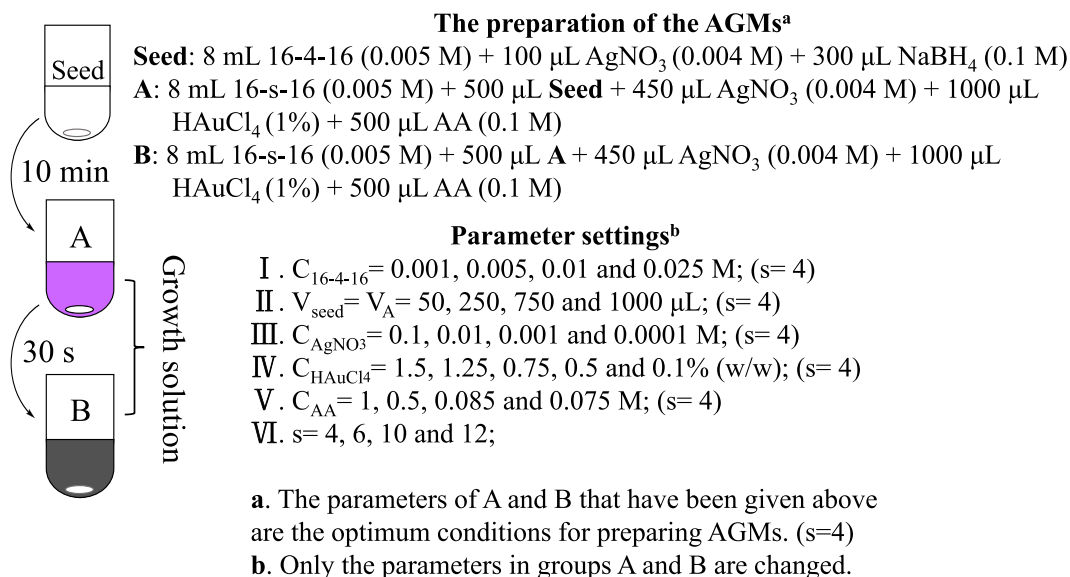
Synthesis of the RhB-tagged AGMs

To evaluate the SERS performance, 175 μL of RhB with different concentrations ranging from 10^{-5} to 10^{-7} M was mixed together with 175 μL of concentrated AGM solutions, and the solutions were subjected to ultrasonic oscillation for 10 s. After mixing, the solutions were incubated for 24 h. The SERS substrate was prepared by dropping 15 μL of the mixed solution onto square silica plates (5 mm × 5 mm), and the solvent was allowed to evaporate in ambient conditions.

Results and discussion

The Ag seeds were characterized to verify their sizes (see Fig. S1). The TEM images revealed that the Ag seeds were 2–5 nm in diameter with a spherical shape. The UV-vis absorption spectrum of the Ag seed solution shows a single absorption band at ~470 nm, which further confirmed the spherical morphology of the seed crystals.

The AGMs were synthesized using a seed-mediated growth method with a low concentration of gemini surfactant. The low- and high-magnification TEM images of typical AGMs are shown in Fig. 1a, b, respectively. These images show that the AGMs were uniform in morphology and size with a diameter of approximately 384 nm, as measured using the SEM images. The

The preparation of the AGMs[a]

Seed: 8 mL 16-4-16 (0.005 M) + 100 μL AgNO$_3$ (0.004 M) + 300 μL NaBH$_4$ (0.1 M)

A: 8 mL 16-s-16 (0.005 M) + 500 μL **Seed** + 450 μL AgNO$_3$ (0.004 M) + 1000 μL HAuCl$_4$ (1%) + 500 μL AA (0.1 M)

B: 8 mL 16-s-16 (0.005 M) + 500 μL **A** + 450 μL AgNO$_3$ (0.004 M) + 1000 μL HAuCl$_4$ (1%) + 500 μL AA (0.1 M)

Parameter settings[b]

Ⅰ. $C_{16\text{-}4\text{-}16}$= 0.001, 0.005, 0.01 and 0.025 M; (s= 4)

Ⅱ. V_{seed}= V_A= 50, 250, 750 and 1000 μL; (s= 4)

Ⅲ. C_{AgNO_3}= 0.1, 0.01, 0.001 and 0.0001 M; (s= 4)

Ⅳ. C_{HAuCl_4}= 1.5, 1.25, 0.75, 0.5 and 0.1% (w/w); (s= 4)

Ⅴ. C_{AA}= 1, 0.5, 0.085 and 0.075 M; (s= 4)

Ⅵ. s= 4, 6, 10 and 12;

a. The parameters of A and B that have been given above are the optimum conditions for preparing AGMs. (s=4)

b. Only the parameters in groups A and B are changed.

Scheme 1 Schematic illustration of the experimental procedure

images show that the surfaces of the AGMs were densely covered with spike-like tips. The tips and the corners between the tips could be easily distinguished (Figs. 1b and 2b).

The chemical composition and crystallinity of the products were determined using XRD and SAED. The XRD patterns of the AGMs are presented in Fig. 1e. Four characteristic diffraction peaks at 38.27°, 44.42°, 64.70° and 77.61° were indexed and correlated well to the (111), (200), (220) and (311) crystal planes of the face-centred cubic (fcc) structure of metallic gold (JCPDF no. 04-0784). The appearance of these peaks indicated that the AGM was polycrystalline. Peaks for other impurities were not observed in the diffraction patterns, indicating that the products were composed of pure crystalline gold. The structural characteristics of the AGMs were further characterized using SAED. The SAED (Fig. 1c) pattern also confirmed that the AGM was polycrystalline. The innermost directional ring was attributed to the (111) plane. The extra rings similarly represented the (200), (220) and (311) planes, which are also shown in the XRD results.

The composition of the AGM was analysed using EDS. As shown in Fig. 1d, the sample was mostly composed of metallic gold, and some bromine and nitrogen were present. The presence of bromine and nitrogen also indicated that the 16-4-16 molecules adsorbed on the crystal surface. The presence of the gemini surfactant may have explained why the product did not aggregate and remained stable for a long time.

Figure 1f presents the corresponding UV-vis-NIR spectra of the AGMs. Compared with the single narrow absorption bands of the gold nanoparticles, the AGMs exhibited broadly extendable absorption features at 748 and 1145 nm, which enables their use in biomedical applications. The tips on the AGM surface enhanced the broad absorbance.

Effects of the 16-4-16 concentration

Surfactants play a significant role in the seed-mediated growth method. When the concentration of the surfactant changes, the products are directly influenced. Figure 2 shows the SEM images and UV-vis spectra corresponding to the concentrations of 16-4-16 used throughout the growth process: 0.001, 0.005, 0.01 and 0.025 M (keeping other factors constant). The SEM images show that the morphology of the gold particles changed with the increasing surfactant concentration, with nearly all other factors held constant. When the concentration of 16-4-16 was 0.001 M, only irregular nanoparticles were observed. However, after careful observation, we determined that these irregular nanoparticles were an assembly of a number of rod-like twigs rather than irregular spherical particles. When the surfactant concentration was increased to 0.005 M, exceptionally uniform AGMs were formed, covered with a uniform distribution of many short tips. While these tips were only a few nanometres long, their edges were clearly sharp, and

Fig. 1 **a**, **b** TEM, **c** SAED, **d** EDS, **e** XRD and **f** UV-vis-NIR spectra of the AGMs
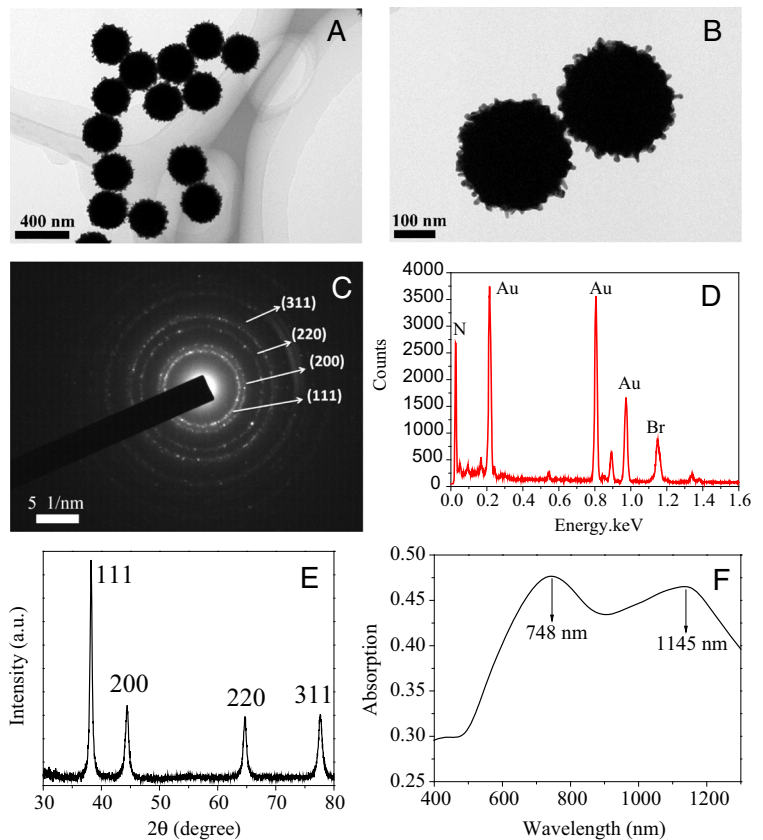
the tips clearly increased the roughness of the particle surface. When the concentration was increased to 0.01 and 0.025 M, the products began to undergo significant changes in both their structure and size. Although the structures of the products were also irregular, the branches outside of the microstructure surfaces were longer and sharper. Interestingly, at this concentration, the tips outside of the product changed into lamellar branches; this phenomenon was not observed in the previous products. As the size of the products increased, the tips on their surfaces became longer petal-like branches. An ideal concentration of 0.005 M 16-4-16 produced a high yield of AGMs with a uniform morphology.
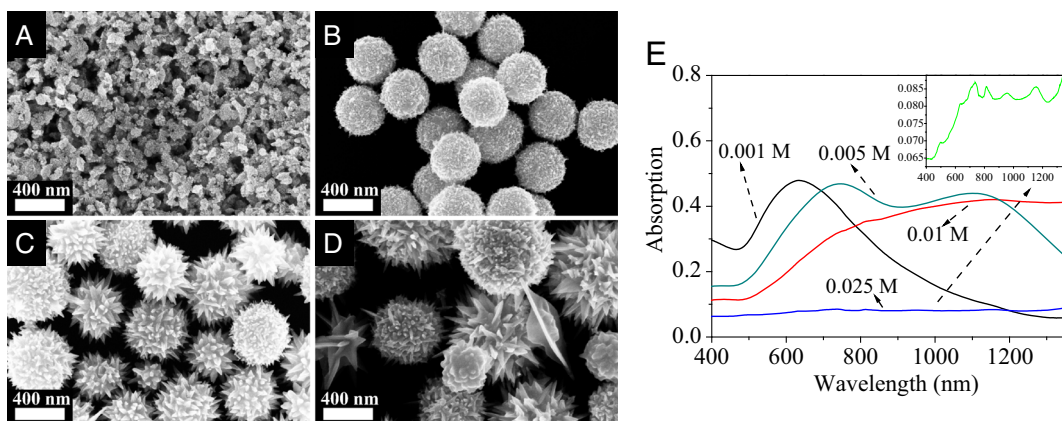

Fig. 2 SEM images of the Au microstructures synthesized with different concentrations of 16-4-16 at **a** 0.001, **b** 0.005, **c** 0.01 and **d** 0.025 M. *Scale bar* = 400 nm. **e** Normalized UV-vis-NIR spectra

Figure 2e presents the corresponding UV-vis-NIR spectra of the products after varying the concentration of 16-4-16. Since the LSPR is closely related to the size and shape of gold nanostructures (Kelly et al. 2003), the LSPR absorption peak of the gold microstructures in the UV-vis-NIR region changed significantly when the concentration of the surfactant was changed. With the increase in concentration, the position of the maximum absorption peak gradually moved to the NIR region, from 650 to 1350 nm, which is consistent with the change of the tips on the surface. When the concentration increased from 0.001 to 0.005 M, the single absorption peak of the products (650 nm) evolved into two peaks (748 and 1145 nm); at higher concentrations (0.01 M or 0.025 M), sharp branches could be observed, and there was a strong absorption peak that extended from 400 to 1350 nm.

As suggested in previous studies, when the concentration of 16-4-16 was 0.005 M, which was slightly higher than its CMC (Singh and Tyagi 2014), the micelles formed at this concentration were mostly spherical, providing a soft template for the formation of gold spherical microstructures. However, as shown in Scheme 2, when the surfactant concentration was just 0.001 M, its concentration was below the threshold for the formation of spherical micelles, no distinctive micelle morphology was observed, and the product was disorganized. At higher concentrations (0.01 and 0.025 M), lamellar micelles were formed. According to the formation mechanism that we summarized, the solid cores and tips produced were formed in two steps. When the spherical cores were formed, the lamellar micelles potentially helped the spike-like protrusions form on the spherical surface. This is in agreement with the characteristics of surfactants that favour the formation of lamellar micelles at high concentrations and the formation of spherical micelles at low concentrations (Figueira-Gonzalez et al. 2013; Graciani et al. 2010). In summary, high surfactant concentrations were conducive to controlling the synthesis of lamellar-like nanostructures, while lower concentrations favoured the synthesis of spherical nanostructures. Therefore, the presence of 16-4-16 is exceptionally important for regulating the structures of the synthetic gold nanomaterials.

Effect of the amount of Ag seeds

Seeds play a crucial role in the seed-growth method, and the amount of seeds may be one of the most influential factors. To explore the effect of the seed dosage on the formation of the AGMs, keeping the other factors constant, the Ag seed volumes used (including the amount of solution from A to B) were 50, 250, 750 and 1000 μL. As shown in Fig. 3, with the increase in the amount of Ag seeds, the most obvious phenomenon was the change in the particle size, which changed from 800 ± 11 to 403 ± 4, 290 ± 4 and 382 ± 4 nm, respectively (as listed in Table 1).

As seen from Fig. 3a–c, when the volume of Ag seeds changed from 50 to 750 μL, the AGMs exhibited good monodispersity, and the size gradually decreased. When the volume of Ag seeds was 50 μL, the average size of the product was the largest, while the sizes of the other three groups were close to each other. Different from the other three products, the size increased when the volume of Ag seeds was 1000 μL, but the product was not a good dispersion. Clearly, various particle sizes were observed (Fig. 3d).

Figure 3e shows the UV-vis-NIR spectra of the products after varying the amount of Ag seeds used. When the volumes of the Ag seeds were 50, 250 and 1000 μL, the products exhibited strong absorption peaks in both the visible and NIR regions, extending from 500 to 1350 nm, which were closely related to the high density of the tips on the product surfaces. However, when the seed volume was 750 μL, the product had a strong absorption peak at approximately 932 nm because the smaller size of the product resulted in a lower density of tips. Therefore, the spherical core played a dominant role in the absorption of light in the band at approximately 932 nm.

The amount of Ag seeds relative to the concentration of gold nanoparticles (which were derived from the reduction of $HAuCl_4$ using AA) greatly affected the particle size. When less seeds were added to the reaction system, the ratio of gold nanoparticles to the seeds was high, and the gold nanoparticles accumulated and grew rapidly with Ag seeds as the centre, resulting in a larger product size. In contrast, a small ratio of gold nanoparticles to Ag seeds resulted in a smaller particle size. However, the uneven product sizes observed when the volume of Ag seeds was 1000 μL was attributed the excessive amount of Ag seeds greatly reducing the distances between the seeds. This distance reduction led to aggregation due to the high surface energy of the Ag seeds before they grew into AGMs, resulting in an unequal distribution of seeds and gold nanoparticles. Then, the seeds became more distributed and

Scheme 2 The possible structures of 16-4-16 and the products formed as a function of the concentration
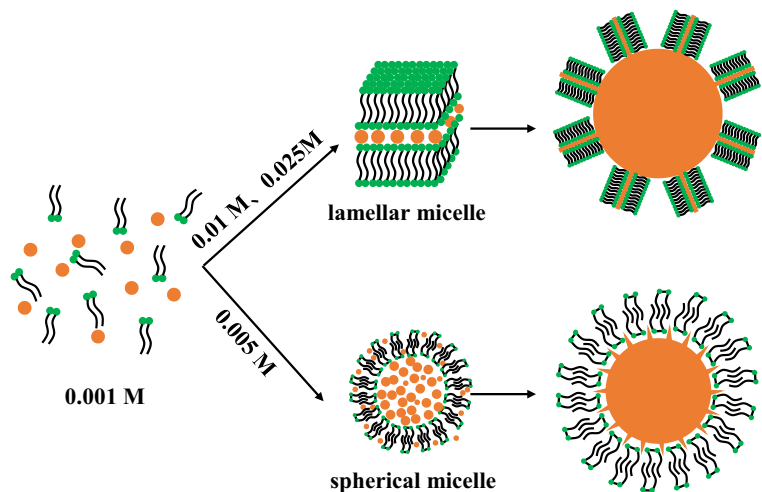
gathered more gold nanoparticles to form larger particle sizes, and vice versa, which resulted in a large difference in the size distribution of the product.

Effect of the AgNO₃ feed concentration

$AgNO_3$ is widely used as a feed input to regulate the morphology of nanomaterials. The vast majority of studies have shown that changes in the $AgNO_3$ concentration can lead to significant changes in the morphology of the product. Figure 4 shows the results of changing the concentration of $AgNO_3$ from 0.1, 0.01, 0.001 to 0.0001 M while maintaining the other factors as constants. Consistent with most of the literature, the change in the concentration of $AgNO_3$ had a significant effect on the product morphology.

As shown in Fig. 4a, when the concentration of $AgNO_3$ was 0.1 M, all the products were small spherical particles (as shown in Table 1, the average size was approximately 205 ± 2 nm) with a few short tips on the surface. When the concentration was reduced to 0.01 M, the particle size and density of the tips increased, while small sections of the particles were bare (Fig. 4b). Upon further decreasing the $AgNO_3$ concentration to 0.001 M, the particle dispersion became uneven. Many small particles were present, which reduced the average size of the particles (Fig. 4c). Surprisingly, when the concentration of $AgNO_3$ was reduced to 0.0001 M, as shown in Fig. 4d, the surface of the product became rugged, but the surface of each particle was smooth. Compared with the above, the average size of the particles increased, which was attributed to the irregular edges of the irregular particles.
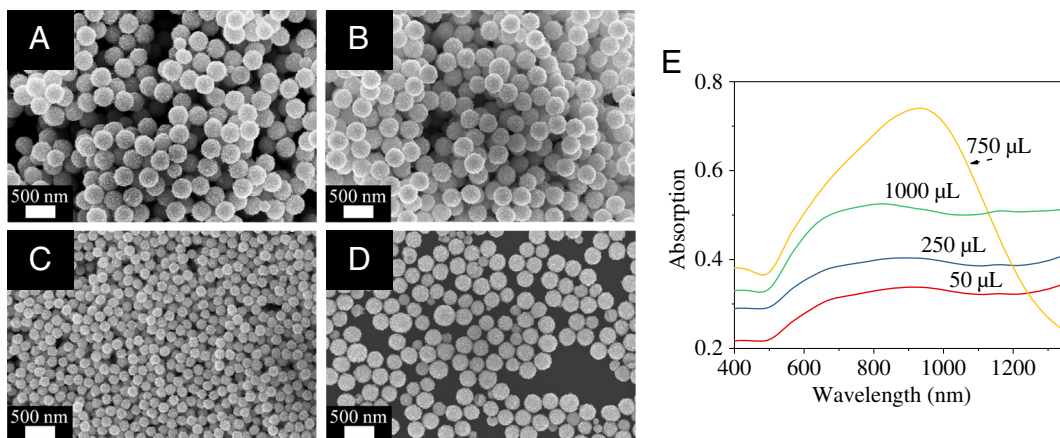

Fig. 3 SEM images of the Au microstructures synthesized with different amounts of Ag seed at **a** 50, **b** 250, **c** 750 and **d** 1000 μL. *Scale bar* = 500 nm. **e** Normalized UV-vis-NIR spectra

Table 1 Summary of the average diameters and concentrations of the gold nanoparticles synthesized under different reaction conditions

Group	Sample	$C_{16\text{-}4\text{-}16}$ (M)	0.005 M 16-s-16	CMC[c] (mM)	V_{seed} (μL)	$C_{AgNO_3 feeding}$ (M)	C_{HAuCl_4} (%)	C_{AA} (M)	Average diameter (nm)[a]	$C_{nanoparticles}$ ($\times 10^{-12}$ M)[b]
I	1	0.001			500	0.004	1	0.1	130 ± 3	21,520.00
	2	0.005			500	0.004	1	0.1	384 ± 3	4.62
	3	0.01			500	0.004	1	0.1	388 ± 5	4.48
	4	0.025			500	0.004	1	0.1	587 ± 2	1.30
II	1	0.005			50	0.004	1	0.1	800 ± 11	0.51
	2	0.005			250	0.004	1	0.1	403 ± 4	4.00
	3	0.005			750	0.004	1	0.1	290 ± 4	10.72
	4	0.005			1000	0.004	1	0.1	382 ± 4	4.70
III	1	0.005			500	0.1	1	0.1	205 ± 2	30.40
	2	0.005			500	0.01	1	0.1	328 ± 5	7.42
	3	0.005			500	0.001	1	0.1	192 ± 3	37.04
	4	0.005			500	0.0001	1	0.1	458 ± 14	2.73
IV	1	0.005			500	0.004	1.5	0.1	432 ± 7	4.87
	2	0.005			500	0.004	1.25	0.1	352 ± 5	7.50
	3	0.005			500	0.004	0.75	0.1	252 ± 5	12.24
	4	0.005			500	0.004	0.5	0.1	241 ± 4	9.36
	5	0.005			500	0.004	0.1	0.1	191 ± 5	3.76
V	1	0.005			500	0.004	1	1	327 ± 6	7.49
	2	0.005			500	0.004	1	0.5	419 ± 9	3.56
	3	0.005			500	0.004	1	0.085	335 ± 9	6.97
	4	0.005			500	0.004	1	0.075	268 ± 3	9.36
VI	1		16-4-16	0.027	500	0.004	1	0.1	384 ± 3	4.62
	2		16-6-16	0.043	500	0.004	1	0.1	757 ± 7	0.60
	3		16-10-16	0.027	500	0.004	1	0.1	590 ± 6	1.27
	4		16-12-16	0.020	500	0.004	1	0.1	352 ± 6	6.01

[a] The data of the average particle sizes of all the particles were obtained from DLS measurements

[b] The concentration of the gold nanoparticle solution was calculated using the following equation:

$$C = \frac{N_{Total}}{N_E V N_A}$$

where N_{Total} is the total number of gold atoms added to the reaction solution, N_E is the number of gold atoms present in each nanoparticle, V is the volume of the product solution and N_A is the Avogadro's constant. The volume of each particle is represented by the volume of the sphere calculated from the average particle size

[c] Data were derived from De et al. (1996)

Figure 4e shows the corresponding UV-vis-NIR spectra of the products after varying the AgNO$_3$ concentration. When the concentration of AgNO$_3$ was 0.1 M, the only significant absorption peak was observed at a wavelength of approximately 716 nm, indicating that the corresponding product contained small spherical particles with a small tip density. However, similar to the AGMs, the product exhibited a continuous absorption peak only in the range of 500 to 1350 nm when the AgNO$_3$ concentration was 0.01 M. When the concentration decreased to 0.001 and 0.0001 M, the corresponding UV-vis absorption peak exhibited an apparent absorption peak only between 700 and 900 nm with a long tail that extended into the NIR region as the product became inhomogeneous or rugged.

The fact that the adsorption of Ag nanoparticles at the seed surface active sites led to the formation of AGMs may be consistent with the above phenomenon. The
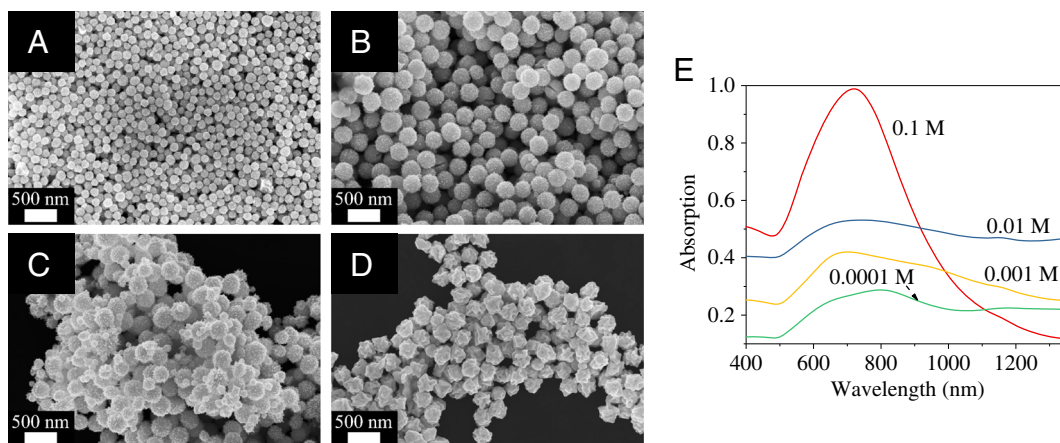
Fig. 4 SEM images of the Au microstructures synthesized with different concentrations of $AgNO_3$ at **a** 0.1, **b** 0.01, **c** 0.001 and **d** 0.0001 M. *Scale bar* = 500 nm. **e** Normalized UV-vis-NIR spectra

activity of Ag is higher than that of Au. After AA was added to the system, $AgNO_3$ first reduced into small Ag nanoparticles and then attached to the active sites of the seed surfaces. Then, multiple substitution reactions occurred with $HAuCl_4$, leading to the formation of the AGM morphology. This is consistent with the experimental results above, that is, when the concentration of the $AgNO_3$ feed was high, such as 0.1, 0.01, and 0.001 M, more Ag^+ became distributed around the seeds to form more tips on the product surfaces. Therefore, when the $AgNO_3$ concentration was 0.1 M, higher concentrations of $AgNO_3$ could adsorb onto more active sites and cause the reaction to occur more quickly, resulting in smaller products. In addition, when the concentration gradually decreased to 0.01 and 0.001 M, products with large sizes and uneven distributions were obtained due to the decrease in the active site adsorption and the unequal distribution of $AgNO_3$. However, when the concentration was only 0.0001 M, the small amount of Ag^+ could not evenly distribute around the spherical Ag seeds. The Ag^+ could only distribute at a few locations around the seed, and the resulting product exhibited a smooth surface with a few rough areas.

Effect of the $HAuCl_4$ concentration

As we all know, the change in the concentration of a raw material has a great impact on the product. Moreover, the charge of the $AuCl_4^-$ anion formed by the aqueous solution of $HAuCl_4$ was opposite to that of the quaternary ammonium gemini surfactant; therefore, the change in the concentration of $HAuCl_4$ had a great

influence on the product. Figure 5 shows the results of changing the concentration of $HAuCl_4$ from 1.5 to 1.25, 0.75, 0.5 and 0.1% (*w/w*), while the other factors remained the same. Obviously, with the increase in the concentration of $HAuCl_4$, the product gradually evolved from spherical structures to AGMs, open-mouthed submicrostructures and ribbon nanowires.

When the concentration of $HAuCl_4$ was 1.5%, as shown in Fig. 5a, the product was roughened spherical microparticles with a good dispersion. When the concentration of $HAuCl_4$ gradually decreased from 1.25 to 0.75 and 0.5%, as shown in Fig. 5b–d, the average diameter of the particles decreased gradually, and the surface of the product changed greatly. As shown in Fig. 5b, the product had a better distribution of AGMs, and each particle surface had densely distributed tips. However, the length and density of the tips on the surface of the particles became significantly increased and many particles had bare areas when the concentration was 0.75 or 0.5%; these products did not exhibit good dispersions (Fig. 5c, d). In particular, as shown in Fig. 5e, when the concentration of $HAuCl_4$ was reduced to 0.1%, the product was completely transformed into ribbon nanowires with a diameter of only tens of nanometres and a length of a few microns, and other products were not observed.

The information provided by SEM was verified from the UV-vis-NIR spectra for the products presented in Fig. 5f. When the concentration of $HAuCl_4$ was 1.5%, the only absorption peak of the spherical product was located at approximately 720 nm, which was the characteristic absorption peak of the rough gold microspheres. When the concentrations were 1.25, 0.75 and
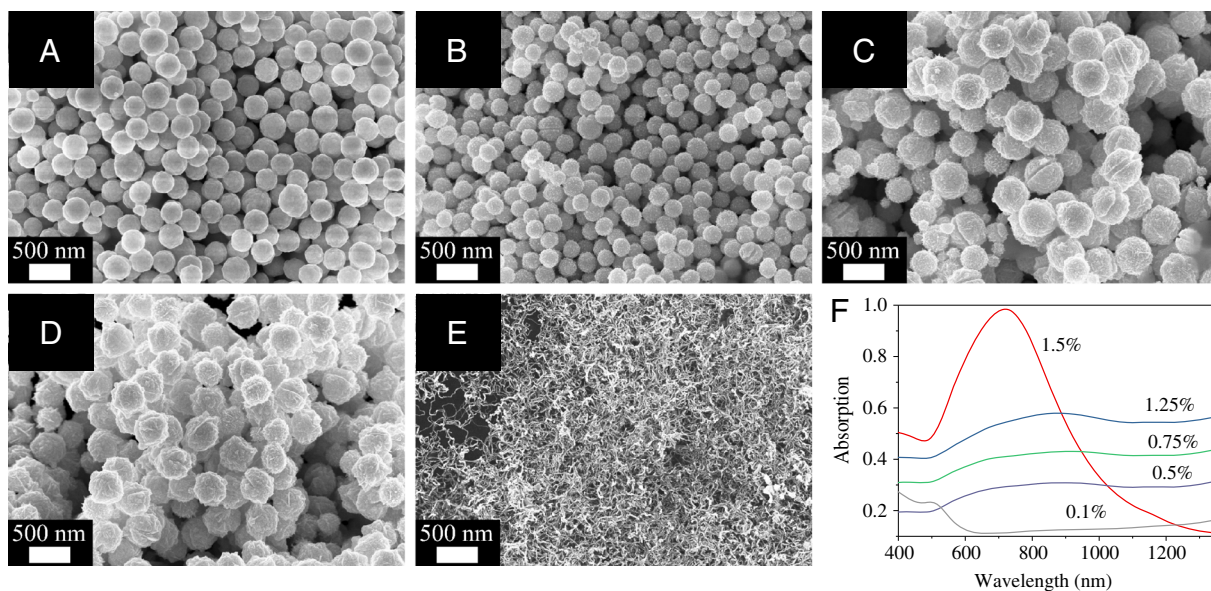
Fig. 5 SEM images of the Au microstructures synthesized with different concentrations of HAuCl₄ at **a** 1.5, **b** 1.25, **c** 0.75, **d** 0.5 and **e** 0.1%. *Scale bar* = 500 nm. **f** Normalized UV-vis-NIR spectra

0.5%, the position of the maximum absorption peak extended into the NIR region. The products presented a strong absorption peak in the range of 500–1350 nm, which was closely related to the long and high density of the tips or sharp edges. However, when the concentration was 0.1%, the UV-vis spectrum of the nanowires was significantly different with the others, and the only strong absorption peak was located at approximately 502 nm.

The above phenomenon may have been directly related to the electrostatic forces between the cationic quaternary ammonium gemini surfactant and the $AuCl_4^-$ anions (Wang et al. 2013a, b, c). When the concentration of HAuCl₄ was 1.5%, the high concentration of $AuCl_4^-$ anions and 16-4-16 resulted in strong electrostatic interactions that prevented the surfactant molecules from forming stable micelles and 16-4-16 from acting as a soft template. In addition, the gold nanoparticles formed by the reduction of AA rapidly formed spherical particles due to the high surface energy. However, when the concentrations of $AuCl_4^-$ anions and 16-4-16 were in the appropriate range, concentrations of 1.25, 0.75 and 0.5%, the electrostatic repulsions between the molecules of 16-4-16 enabled the formation of suitable soft templates, such as spherical micelles, promote the formation of AGMs and open-mouthed shapes. However, a lower concentration of HAuCl₄ (C = 0.1%) would cause 16-4-16 to form banded

aggregates, leading to the formation of ribbon nano-wires. This result indicated that high concentrations of HAuCl₄ were not conducive to the production of thorns, while low concentrations of HAuCl₄ favoured of one-dimensional structures, such as nanowires. Only certain concentration ranges of HAuCl₄ enabled the formation of regular AGMs.

Effect of the concentration of AA

AA is a mild organic reducing agent that is commonly used for synthesizing nanomaterials. Compared with other reducing agents, AA can maintain a stable reduction rate, which can be conducive to the growth of a regular morphology. This behaviour reflects the importance of selecting the appropriate type of reducing agent and controlling the rate of reduction to control the synthesis of nanomaterials. We used different concentrations of AA, 1, 0.5, 0.085 and 0.075 M, to reduce HAuCl₄ to prepare gold micromaterials, without altering the other experimental factors. Figure 6 shows the corresponding SEM and UV-vis-NIR spectra of these products.

As the concentration of AA gradually decreased, the product regularly changed from bricks to AGMs to spheres. When the AA concentration was 0.5 M, the product contained bricks with sharp edges mixed with a few gold nanoplates (Fig. 6a). When the AA
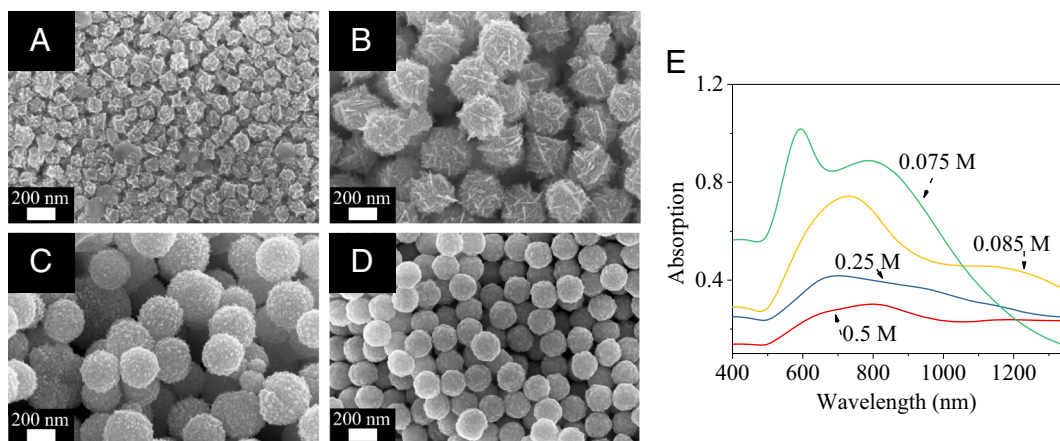
Fig. 6 SEM images of the Au microstructures synthesized using different concentrations of AA at **a** 0.5, **b** 0.25, **c** 0.085 and **d** 0.075 M. *Scale bar* = 200 nm. **e** Normalized UV-vis-NIR spectra

concentration was reduced to 0.25 M, the product changed from bricks into spherical particles (Fig. 6b) with many sharp edge protrusions on the surface, which was unlike other products with only a few tips. When the AA concentration continued to decrease, as shown in Fig. 6c, d, the product gradually became regular spherical shapes, and the sharp edges disappeared. When the AA concentration was 0.085 M, the product size was larger, and the surface had many long tips, but when it was 0.075 M, the particle size was small, and the product appeared to be more rounded without prominent tips on the surface.

Figure 6e presents the corresponding UV-vis-NIR spectra. In the UV-vis-NIR spectra, the absorption bands of the products are different. When the AA concentration was high (0.5 and 0.25 M), the products had sharp edges, resulting in a continuous absorption peak in the range of 500–1350 nm, but due to the uneven distribution of the product surface tips, the intensity of the absorption peak gradually decreased after 800 nm. Clearly, the product exhibited tips when the concentration of AA was 0.085 M. The corresponding absorption peak moved closer to the NIR region, resulting in the product that exhibited two significant absorption peaks at 750 and 1150 nm. In contrast, the spherical particles with a smooth surface only absorbed at 600 and 800 nm when the concentration of AA was just 0.075 M.

The reason for the above phenomenon was attributed to the reaction speed. As shown above, when the concentration of AA was 0.5 M, the high concentration of AA rapidly reduced $HAuCl_4$ into smaller gold nanoparticles. Since the surface energy of the smaller particles was higher, the rapid aggregation of these small

nanoparticles in the solution was conducive to the formation of sharp edges. Additionally, since the aggregation rate of these nanoparticles was fast, the product could not assemble into regular spherical shapes. This conjecture was verified when the AA concentration gradually decreased from 0.25 to 0.085 and 0.075 M; the product tended to form regular spherical particles, and the sharp edges changed into tips or became smooth. The reason for this change was the slow aggregation rate of the nanoparticles with a lower surface energy. Thus, a suitable aggregation rate and a moderate reduction rate favoured the formation of nanoparticles with a regular morphology.

Effect of the spacer length of the gemini surfactants

In addition to changing the concentration of 16-4-16, changing the gemini surfactant type also had an important influence on the results when all other parameters were held constant. Scientific research has shown that the structure of micelles is also closely related to the spacer length of gemini surfactants (Bhattacharya and Biswas 2011) Figure 7a–e presents the effects of changing the gemini surfactant type (16-s-16, s = 4, 6, 10 and 12) on the formation of the AGMs, keeping the other conditions constant. Interestingly, the gold microstructures exhibited good monodispersity regardless of the type of gemini surfactant used. In comparison, as shown in Fig. S2, when CTAB was used as the stabilizer, the product was mostly random spherical particles. However, the product sizes increased approximately with the increase in the spacer length, and the tip density changed. When the carbon number of the spacer length was 4 or 12, the tip density

on the surface of the products was high, and the distribution of the thorns was uniform. In particular, the use of 16-10-16 resulted in particle surfaces with almost indistinguishable protrusions, similar to a spherical particle. Additionally, the products synthesized with 16-6-16 appeared as spheres with dense short tips that were taller than those of the other products.

Figure 7e shows the corresponding UV-vis-NIR spectra after varying the gemini surfactant type. The products synthesized using the four types of surfactants exhibited strong absorption peaks in the range of 500–1300 nm. When the spacer length was 4 or 10, the absorption of the product exhibited two absorption bands at approximately 700 nm and 1050 nm, and strong absorption occurred at 500–1300 nm for a spacer length of 6 or 12. Comparing the two sets of spacer lengths, the absorption peaks of the higher spacer length products (6 or 12) decreased at a certain wavelength, but the products using shorter spacer lengths (4 or 10) maintained high absorption in the 600–1300-nm continuous region.

A brief representation of the possible influences of 16-s-16 (s = 4, 6, 10 and 12) is shown in Scheme 3. When the surfactant concentration was low, spherical micelles were formed. The hydrophobic interactions and charge repulsions due to the quaternary ammonium salts (Chen 1986) provided space between the gemini surfactant molecules for the tips to grow between the hydrophobic chains. When s was below 10, the spacer was stretched at the air-water interface; when s was 10 or 12, the spacer became too hydrophobic to remain in contact with water and adopted a folded, archway-like conformation (Alami et al. 1993). In addition, longer gemini surfactant spacer lengths brought the surfactant

molecules closer in a crisscross pattern on the surface of the micelles. This pattern narrowed the intermolecular gap, preventing the reduced gold nanoparticles from depositing on the surface of the spherical gold core. However, when the intermediate chains were too long (16-12-16), they reacted with the tails to repel the water phase and again provided space for gold nanoparticle deposition, as shown in the SEM image in Fig. 3d; the product surfaces became very rough with different lengths of tips.

Mechanism of the morphological transformation

We oversaw the formation of the crystals by removing the solution in group B at different time points during the reaction for SEM analysis. Figure 8 presents the SEM and UV-vis images of the intermediate products observed. Slightly different from previously reported mechanisms, we believe the growth process of the AGMs occurred in two stages. The first stage was to gradually form a uniform solid core consisting of gold nanoparticles, and the second stage was the generation of gold tips on the surface of the core to combine into the acanthosphere-like morphology.

During this process, the AGMs were synthesized through a two-step, seed-mediated growth method. In the first step, after the reactants were injected into the solution, silver nanoparticles dissolved into Ag^+ along with the migration of electrons. This dissolution caused a galvanic replacement reaction between the silver nanoparticles and $HAuCl_4$ and led to the formation of small spherical gold nanoparticles (Sun and Xia 2002). This reaction occurred because the reduced small gold
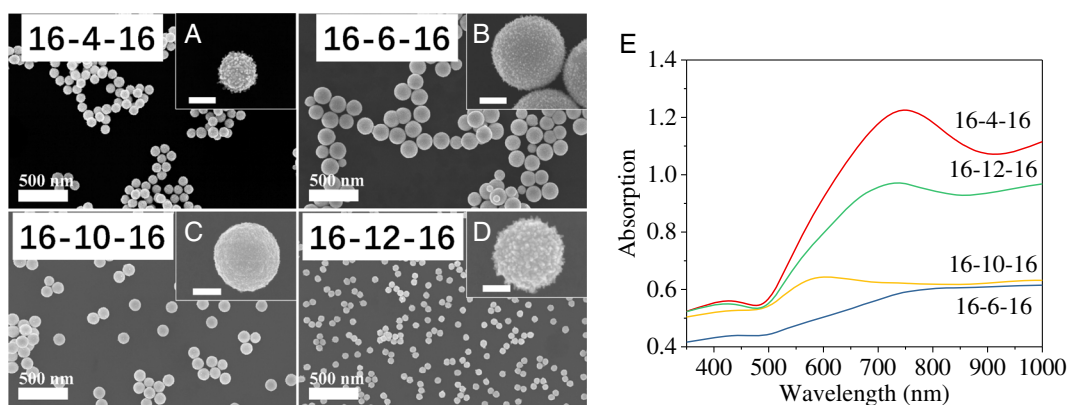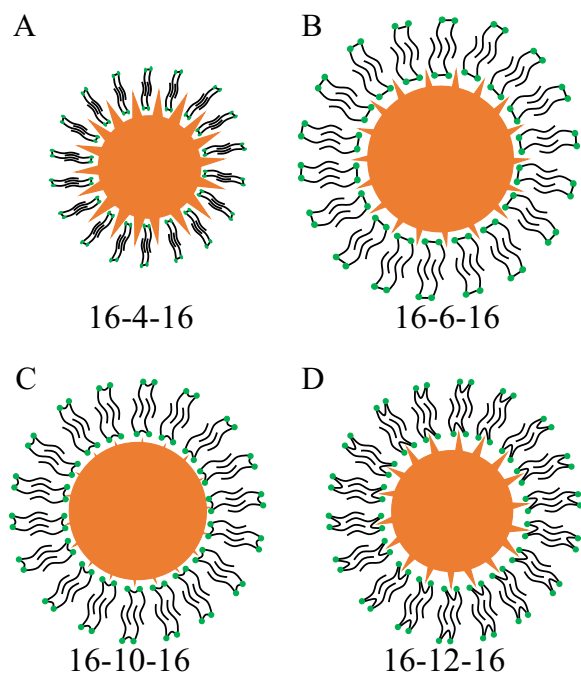

Fig. 7 SEM images of the Au microstructures synthesized using a series of gemini surfactants at a 16-4-16, b 16-6-16, c 16-10-16 and d 16-12-16. Scale bar = 500 nm; inset scale bar = 200 nm. e Normalized UV-vis-NIR spectra

Scheme 3 An illustration of the effects of the spacer length of the gemini surfactant on the formation of the products

considered to be the growth process of the cores. As the reaction proceeded for 1 min, Au^{3+} was reduced to Au metal due to the AA and grew on the newly formed cores. In addition to growth via atomic addition, the cores could directly coalesce into larger crystals via a particle-mediated aggregation process (Kulak et al. 2007). Defects can be observed on the intermediate products in Fig. 8a–c. A large number of defects on the particles could act as sites for further Au precipitation (Wang et al. 2012). When the reaction time was gradually increased to 10 min, the Au core grew into primary nanoparticles and aggregated to form microspheres to reduce the total energy of the system. Various types of quasispherical nanoparticles gradually became spherical particles that were uniform in size. By comparing Fig. 8d–f with the previous analyses, we found that the growth of each particle did not occur simultaneously; the particles grew gradually until they had the same size and morphology. Obviously, after growing for 3 min, quasispherical particles with poor dispersibility sequentially became spherical. Compared with the results after 3 min of growth, after growing for 10 min, the most noticeable change was that the sizes of the microspheres became consistent. Simultaneously, the number of particles decreased significantly. This result may have been due to an Ostwald ripening process (Ostwald 1900), which was driven by the increasing chemical potential of the NPs due to particle dissolution and ion reprecipitation, leading to an increase in the particle size but a decrease in the number of particles. Later, a few tips on the spherical gold particles
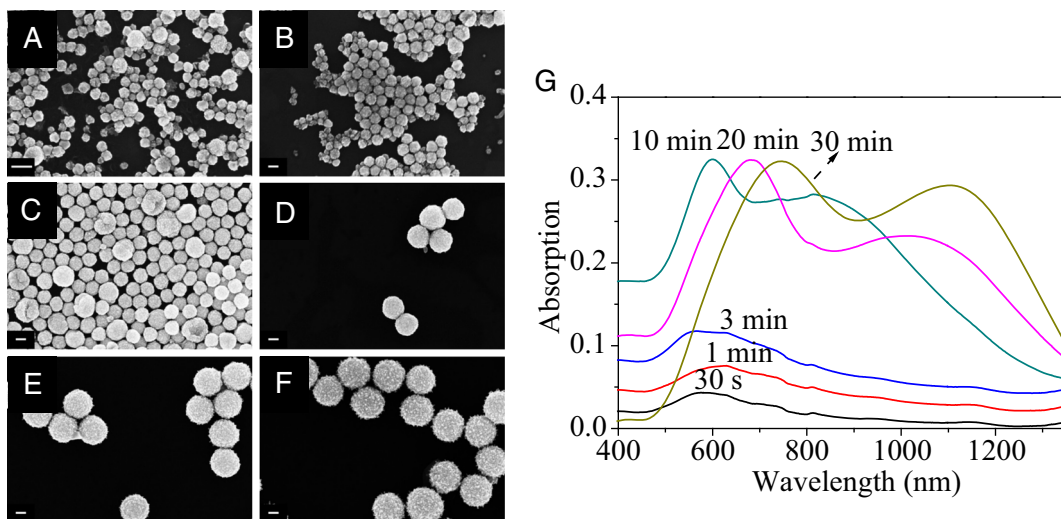
nanoparticles had a tendency to nucleate on the surfaces of the silver NPs to lower the energy cost. In the second step, the growth process of the AGMs began to occur; we started the timer after all the reagents were added into the system. As shown in Fig. 8, after all reactants were combined for 30 s, a series of quasispherical Au NPs with different sizes was obtained (Fig. 8a), which was

Fig. 8 SEM images of the intermediate products of the Au nanoparticles obtained at different reaction times at **a** 30 s, **b** 1 min, **c** 3 min, **d** 10 min, **e** 20 min and **f** 30 min. *Scale bar* = 100 nm. **g** Normalized UV-vis-NIR spectra of the intermediate products

could be detected using the 16-4-16 molecules, which indicated the formation of the acanthosphere-like morphology. After 20 min, the acanthosphere-like morphology could be markedly distinguished. Structures with more tips on the surface were produced (Fig. 8e), and the sizes of the particles increased compared with those of the structures obtained after 10 min. Although the AGM morphology was formed within 20 min, well-developed gold microstructures composed of longer tips on the surface were formed after 30 min of reaction time. Possibly due to silver underpotential deposition (UPD), Ag (0) and AgBr chemisorbed on the surface of the active sites of the seed particles during the sequential growth of the gold atoms, leading to the formation of multibranched particles (Vijayaraghavan et al. 2016). After the reaction proceeded for 30 min, particles with acanthosphere-like morphologies were formed with larger sizes and longer tips (Fig. 8f). These particles exhibited a better monodispersity than the intermediate particles.

Conclusions supporting the above-described formation process were also obtained from the UV-vis spectra (Fig. 8g). As shown in Fig. 8g, only one absorption peak existed at approximately 600 nm when the reaction occurred from 30 s to 3 min, indicating that AGMs were not formed during this process. When the reaction time was extended to 10, 20 and 30 min, the absorption peak shifted to approximately 748 nm, and a new absorption peak appeared at a longer wavelength (1145 nm, Fig. 1). This result indicates that the tips started to form significantly during this process. From the SEM and UV-vis analyses of the intermediate products isolated at various time points, it is clear that the evolution of the AGMs followed a two-stage growth process. However, the formation mechanisms in our research were not flawless and require further investigation.

Evaluation of the SERS efficiency

Because the gold NPs exhibited morphology- and size-dependent SERS characteristics, the SERS performance of the product was measured using RhB molecules as the absorbent, which is a food additive that can cause cancer. Figure 9 shows the SERS spectra of RhB with concentrations ranging between 5×10^{-6} and 5×10^{-8} M in the presence of aqueous colloidal gold microstructures. The SERS signal intensities were obtained using an Ar^+ laser ($\lambda = 514.5$ nm) as the excitation source. Clearly, from Fig. 9, RhB on the AGMs exhibited intense SERS signals at a concentration of 5×10^{-7} M. The spectrum clearly exhibits
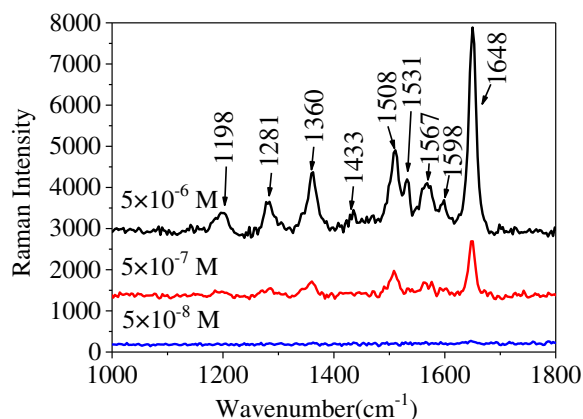

Fig. 9 Raman spectra obtained at different target concentrations (5×10^{-6} M~5×10^{-8} M) of RhB molecules in the presence of AGMs

peaks at approximately 1198, 1281, 1360, 1433, 1508, 1531, 1567, 1598 and 1648 cm^{-1}, which are the pure RhB Raman vibrations in the 1100~1700 cm^{-1} region (Kneipp et al. 1999). The peaks at 1360, 1433, 1508, 1531, 1567 and 1648 cm^{-1} were attributed to aromatic C–C stretching. The peak at 1598, 1281 and 1195 cm^{-1} were due to aromatic C=C stretching, C–C bridge-band stretching and aromatic C–H bending, respectively. RhB Raman features were not found at concentrations of 5×10^{-8} M or lower. There were two mainly reasons for the efficient enhancement of the RhB molecule signals. First, the uneven surface of the AGMs enabled higher RhB molecule adsorption, which consequently lead to strong plasmon coupling with adjacent particles (Ndokoye et al. 2016). Second, the most localized and enhanced electric field areas were found close to the tips, causing strong electric field enhancement (Fang et al. 2010). When using AGMs as a Raman substrate, the short sharp tips around the AGMs created more "hot-spots," which contributed to large electric field enhancement as well as an increase in the Raman signal (Wang et al. 2012). Even though the AGMs produced a strong SERS signal, it is still difficult to precisely calculate the intensity variations as a function of the product sizes using probe molecules (Khoury and Vo-Dinh 2008).

Conclusion

In conclusion, highly monodisperse and uniformly distributed AGMs were synthesized via seed-mediated growth within 30 min using 16-s-16 (s = 4, 6, 10 and 12) at 30 °C. The products exhibited wide absorption bands in the UV-

vis-NIR region, which possessed broadly extendable absorption bands ranging from 500 to 1350 nm. The results showed that the concentrations of 16-4-16, $AgNO_3$, $HAuCl_4$ and AA and the amount of seeds had significant effects on the size, morphology and UV-vis absorption spectra of the products, and the aggregates of the gemini surfactants in the solution were considered to be indispensable for the formation of various morphologies. In particular, changing the 16-4-16 concentration led to changes in the product from irregular shapes to spiked spheres and lamellar spikes. Changing the concentration of $HAuCl_4$ converted the products between open-mouthed submicrostructures, spiked spheres and ribbon nanowires. Meanwhile, changing the spacer length caused the stretching and bending of the spacers between the gemini surfactants to behave differently, which led to the formation of AGMs with different lengths of tips and sizes. The characterization of the formation mechanism indicated that the solid core and the tips on the surface of the AGMs were generated in a two-stage growth process. In addition, the AGMs synthesized under optimal conditions acted as sensitive SERS substrates, and concentrations of 5×10^{-7} M RhB could be detected. This scientific study provides a new train of thought for controlling the morphology and size of multibranched gold nanoparticles with the seed-mediated method. This method may be applicable to the synthesis of other types of nanomaterials.

Compliance with ethical standards

Conflict of interest   The authors declare that they have no conflict of interest.

References

Alami E, Beinert G, Marie P, Zana R (1993) Alkanediyl-.alpha., .omega.-bis(dimethylalkylammonium bromide) surfactants. 3. Behavior at the air-water interface. Langmuir 9:1465–1467

Bakr OM, Wunsch BH, Stellacci F (2006) High-yield synthesis of multi-branched urchin-like gold nanoparticles. Chem Mater 18:3297–3301

Bakshi MS (2016) How surfactants control crystal growth of nanomaterials. Cryst Growth Des 16:1104–1133

Bhattacharya S, Biswas J (2011) Role of spacer lengths of gemini surfactants in the synthesis of silver nanorods in micellar media. Nano 3:2924–2930

Chen L, Ji F, Xu Y, He L, Mi Y, Bao F, Sun B, Zhang X, Zhang Q (2014) High-yield seedless synthesis of triangular gold nanoplates through oxidative etching. Nano Lett 14:7201–7206

Chen Q, Jia Y, Xie S, Xie Z (2016) Well-faceted noble-metal nanocrystals with nonconvex polyhedral shapes. Chem Soc Rev 45:3207–3220

Chen SH (1986) Small angle neutron scattering studies of the structure and interaction in micellar and microemulsion systems. Annu Rev Phys Chem 37:351–399

Cheng L, Ma C, Yang G, You H, Fang J (2014) Hierarchical silver mesoparticles with tunable surface topographies for highly sensitive surface-enhanced Raman spectroscopy. J Mater Chem A 2:4534–4542

De S, Aswal VK, Goyal PS, Bhattacharya S (1996) Role of spacer chain length in dimeric micellar organization. Small angle neutron scattering and fluorescence studies. J Phys Chem C 100:11664–11671

Fang J, Du S, Lebedkin S, Li Z, Kruk R, Kappes M, Hahn H (2010) Gold mesostructures with tailored surface topography and their self-assembly arrays for surface-enhanced Raman spectroscopy. Nano Lett 10:5006–5013

Figueira-Gonzalez M, Francisco V, Garcia-Rio L, Marques EF, Parajo M, Rodríguez-Dafonte P (2013) Self-aggregation properties of ionic liquid 1,3-didecyl-2-methylimidazolium chloride in aqueous solution: from spheres to cylinders to bilayers. J Phys Chem B 117:2926–2937

Gilroy KD, Ruditskiy A, Peng H, Qin D, Xia Y (2016) Bimetallic nanocrystals: syntheses, properties, and applications. Chem Rev 116:10414–10472

Graciani MM, Rodriguez A, Martin VI (2010) Concentration and medium micellar kinetic effects caused by morphological transitions. Langmuir 26:18659–18668

Guerrero-Martinez A, Perez-Juste J, Carbo-Argibay E, Tardajos G, Liz-Marzan LM (2009) Gemini surfactant directed self-assembly of monodisperse gold nanorods into standing superlattices. Angew Chem Int Edit 48:9484–9488

Guo L, Xu Y, Ferhan AR, Chen G, Kim D (2013) Oriented gold nanoparticle aggregation for colorimetric sensors with surprisingly high analytical figures of merit. J Am Chem Soc 135:12338–12345

Hait S, Moulik SP (2002) Gemini surfactants: a distinct class of self-assembling molecules. Curr Sci India 82:1101–1111

Han J, Zhou Z, Yin Y, Luo X, Li J, Zhang H, Yang B (2012) One-pot, seedless synthesis of flowerlike au-Pd bimetallic nanoparticles with core-shell-like structure via sodium citrate coreduction of metal ions. CrystEngComm 14:7036–7042

Jain T, Tehrani-Bagha AR, Shekhar H, Crawford R, Johnson E, Nørgaard K, Holmberg K, Erhart P, Moth-Poulsen K (2014) Anisotropic growth of gold nanoparticles using cationic gemini surfactants: effects of structure variations in head and tail groups. J Mater Chem C 2:994–1003

Jiji SG, Gopchandran KG (2015) Synthesis of gold nanoflowers and their high SERS performance. Mater Today 2:928–933

Ke FS, Solomon B, Ding Y, Xu GL, Sun SG (2014) Enhanced electrocatalytic activity on gold nanocrystals enclosed by high-index facets for oxygen reduction. Nano Energy 7: 179–189

Kelly KL, Coronado E, Zhao LL, Schatz GC (2003) The optical properties of metal nanoparticles: the influence of size, shape, and dielectric environment. J Phys Chem B 107:668–677

Khoury CG, Vo-Dinh T (2008) Gold nanostars for surface-enhanced Raman scattering: synthesis, characterization and optimization. J Phys Chem C 2008:18849–18859

Kneipp K, Kneipp H, Itzkan I, Dasari RR, Feld MS (1999) Ultrasensitive chemical analysis by Raman spectroscopy. Chem Rev 99:2957–2976

Kulak AN, Iddon P, Li Y, Armes SP, Colfen H, Paris O, Wilson RM, Meldrum FC (2007) Continuous structural evolution of calcium carbonate particles: a unifying model of copolymer-mediated crystallization. J Am Chem Soc 129:3729–3736

Li J, Wu J, Zhang X, Liu Y, Zhou D, Sun H, Zhang H, Yang B (2011) Controllable synthesis of stable urchin-like gold nanoparticles using hydroquinone to tune the reactivity of gold chloride. J Phys Chem C 115:3630–3637

Liang JJ, Yang LB, Shen YH, Xie AJ (2008) Synthesis of novel urchin-like architecture Au by self-assembly coupled without template. Mater Res Bull 43:1074–1078

Liu Z, Cheng L, Zhang L, Jing C, Shi X, Yang Z, Long Y, Fang J (2014a) Large-area fabrication of highly reproducible surface enhanced Raman substrate via a facile double sided tape-assisted transfer approach using hollow Au-Ag alloy nanourchins. Nano 6:2567–2572

Liu Z, Cheng L, Zhang L, Yang Z, Liu Z, Fang J (2014b) Sub-100 nm hollow Au-Ag alloy urchin-shaped nanostructure with ultrahigh density of nanotips for photothermal cancer therapy. Biomaterials 35:4099–4107

Liu Z, Yang Z, Peng B, Cao C, Zhang C, You H, Xiong Q, Li Z, Fang J (2014c) Highly sensitive, uniform, and reproducible surface-enhanced Raman spectroscopy from hollow Au-Ag alloy nanourchins. Adv Mater 26:2431–2439

Liu Z, Zhang F, Yang Z, You H, Tian C, Li Z, Fang J (2013) Gold mesoparticles with precisely controlled surface topographies for single-particle surface-enhanced Raman spectroscopy. J Mater Chem C 1:5567–5576

Lu L, Ai K, Ozaki Y (2008) Environmentally friendly synthesis of highly monodisperse biocompatible gold nanoparticles with urchin-like shape. Langmuir 24:1058–1063

Menger FM, Littau CA (1991) Gemini surfactants synthesis and properties. J Am Chem Soc 113:1451–1452

Ndokoye P, Li X, Zhao Q, Li T, Tade MO, Liu S (2016) Gold nanostars: benzyldimethylammonium chloride-assisted synthesis, plasmon tuning, SERS and catalytic activity. J Colloid Interf Sci 462:341–350

Nepal D, Drummy LF, Biswas S, Park K, Vaia RA (2013) Large scale solution assembly of quantum dot-gold nanorod architectures with plasmon enhanced fluorescence. ACS Nano 7: 9064–9074

Niu W, Chua YA, Zhang W, Huang H, Lu X (2015) Highly symmetric gold nanostars: crystallographic control and surface-enhanced Raman scattering property. J Am Chem Soc 137:10460–10463

Ostwald W (1900) Über die vermeintliche Isomerie des roten und gelben quecksilberoxyds und die oberflächenspannung fester Körper. Z Phys Chem 34:495–503

Rengan AK, Bukhari AB, Pradhan A, Malhotra R, Banerjee R, Srivastava R, De A (2015) In vivo analysis of biodegradable liposome gold nanoparticles as efficient agents for photothermal therapy of cancer. Nano Lett 15:842–848

Sabri YM, Kandjani AE, Ippolito SJ, Bhargava SK (2016) Ordered monolayer gold nano-urchin structures and their size induced control for high gas sensing performance. Sci Rep 6: 24625–24634

Sau TK, Murphy CJ (2004) Room temperature, high-yield synthesis of multiple shapes of gold nanoparticles in aqueous solution. J Am Chem Soc 126:8648–8649

Singh V, Tyagi R (2014) Unique micellization and CMC aspects of gemini surfactant: an overview. J Disper Sci Technol 35: 1774–1792

Song C, Wu D, Zhang F, Liu P, Lu Q, Feng X (2012) Gemini surfactant assisted synthesis of two-dimensional metal nanoparticles/graphene composites. Chem Commun 48: 2119–2121

Sun YG, Xia YN (2002) Shape-controlled synthesis of gold and silver nanoparticles. Science 298:2176–2179

Vijayaraghavan P, Liu C, Hwang KC (2016) Synthesis of multi-branched gold nanoechinus using a gemini cationic surfactant and its application for surface enhanced Raman scattering. ACS Appl. Mater. Inter. 8:23909–23919

Wang Z, Ma L (2009) Gold nanoparticle probes. Coordin Chem Rev 253:1607–1618

Wang X, Yang D, Huang P, Li M, Li C, Chen D, Cui D (2012) Hierarchically assembled Au microspheres and sea urchin-like architectures: formation mechanism and SERS study. Nano 4:7766–7772

Wang Y, Yan B, Chen L (2013a) SERS tags: novel optical nanoprobes for bioanalysis. Chem Rev 113:1391–1428

Wang W, Han Y, Gao M, Wang Y (2013b) Template synthesis of braided gold nanowires with gemini surfactant-HAuCl4 aggregates. J Nanopart Res 15:1380–1391

Wang W, Han Y, Tian M, Fan Y, Tang Y, Gao M, Wang Y (2013c) Cationic gemini surfactant-assisted synthesis of hollow Au nanostructures by stepwise reductions. ACS Appl Mater Inter 5:5709–5716

Wu H, Chen C, Huang MH (2009) Seed-mediated synthesis of branched gold nanocrystals derived from the side growth of pentagonal bipyramids and the formation of gold nanostars. Chem Mater 21:110–114

Xu F, Cui K, Sun Y, Guo C, Liu Z, Zhang Y, Shi Y, Li Z (2010) Facile synthesis of urchin-like gold submicrostructures for nonenzymatic glucose sensing. Talanta 82:1845–1852

Xu F, Hou H, Gao Z (2014) Synthesis and crystal structures of gold nanowires with gemini surfactants as directing agents. ChemPhysChem 15:3979–3986

Xu Y, Zhao Y, Chen L, Wang X, Sun J, Wu H, Bao F, Fan J, Zhang Q (2015) Large-scale, low-cost synthesis of monodispersed gold nanorods using a gemini surfactant. Nano 7:6790–6797

You H, Fang J (2016) Particle-mediated nucleation and growth of solution-synthesized metal nanocrystals: a new story beyond the LaMer curve. Nano Today 11:145–167

You H, Ji Y, Wang L, Yang S, Yang Z, Fang J, Song X, Ding B (2012) Interface synthesis of gold mesocrystals with highly

roughened surfaces for surface-enhanced Raman spectroscopy. J Mater Chem B 22:1998–2006

Zaleska-Medynska A, Marchelek M, Diak M, Grabowska E (2016) Noble metal-based bimetallic nanoparticles: the effect of the structure on the optical, catalytic and photocatalytic properties. Adv Colloid Interfac 229:80–107

Zana R, Benrraou M, Rueff R (1991) Alkanediyl-α,ω-bis(dimethylalky1ammonium bromide) surfactants. 1. Effect of the spacer chain length on the critical micelle concentration and micelle ionization degree. Langmuir 7: 1072–1075

Zhou D, Wang R, Zhang M, Weng X, Chen J, Wang A, Feng J (2013) Iron(III) ion-supported electrosynthesis of urchin-like gold arrays. Electrochim Acta 108:390–397